Heliyon 10 (2024) e25298

Contents lists available at ScienceDirect

Heliyon

journal homepage: www.cell.com/heliyon

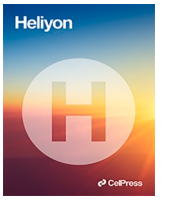

Research article

Online lithium-ion battery intelligent perception for thermal fault detection and localization☆

Luyu Tian [a], Chaoyu Dong [b,*], Yunfei Mu [a], Xiaodan Yu [a], Hongjie Jia [a]

[a] School of Electrical and Information Engineering, Tianjin University, Tianjin, 300072, China
[b] Agency for Science, Technology and Research, Nanyang Technological University, Singapore, 639798

ARTICLE INFO

Keywords:
Lithium-ion battery
Thermal diagnosis
Mask region-based convolutional neural network
Deep learning

ABSTRACT

—Equipping lithium-ion batteries with a reasonable thermal fault diagnosis can avoid thermal runaway and ensure the safe and reliable operation of the batteries. This research built a lithium-ion battery thermal fault diagnosis model that optimized the original mask region-based convolutional neural network based on the battery dataset in both parameters and structure. The model processes the thermal images of the battery surface, identifies problematic batteries, and locates the problematic regions. A backbone network is used to process the battery thermal images and extract feature information. Through the RPN network, the thermal feature is classified and regressed, and the Mask branch is used to ultimately determine the faulty battery's location. Additionally, we have optimized the original mask region-based convolutional neural network based on the battery dataset in both parameters and structure. The improved LBIP-V2 performs better than LBIP-V1 in most cases. We tested the performance of LBIP on the single-cell battery dataset, the 1P3S battery pack dataset, and the flattened 1P3S battery pack dataset. The results show that the recognition accuracy of LBIP exceeded 95 %. At the same time, we simulated the failure of the 1P3S battery pack within 0–15 min and tested the effectiveness of LBIP in real-time battery fault diagnosis. The results indicate that LBIP can effectively respond to online faults with a confidence level of over 98 %.

1. Introduction

With the rapid development of industry, human demand for energy has gradually increased. The drawbacks of traditional energy sources such as coal, petroleum, and other fossil fuels are becoming increasingly apparent. Consuming gasoline, diesel, and other fuels can exacerbate greenhouse gas emissions, contributing to environmental and climate change. Therefore, the emphasis is on achieving the transition from traditional to new energy sources and ensuring sustainable development. With the advancement of technology, sustainable energy sources like photovoltaic and wind power generation have replaced conventional energy sources as the preferred option [1]. However, due to the strong intermittency and volatility of new energy generation, it is necessary to equip energy storage systems to mitigate fluctuations. Additionally, the rapid advancement of electric vehicles has significantly raised the demand for energy storage [2].

☆ This research was supported by National Natural Science Foundation of China (U23B6006, 52277116).

* Corresponding author.
E-mail addresses: tianluyu@tju.edu.cn (L. Tian), dong0120@e.ntu.edu.sg (C. Dong), yunfeimu@tju.edu.cn (Y. Mu), yuxd@tju.edu.cn (X. Yu), hjjia@tju.edu.cn (H. Jia).

https://doi.org/10.1016/j.heliyon.2024.e25298
Received 24 July 2023; Received in revised form 12 January 2024; Accepted 24 January 2024
Available online 30 January 2024
2405-8440/© 2024 Published by Elsevier Ltd. This is an open access article under the CC BY-NC-ND license (http://creativecommons.org/licenses/by-nc-nd/4.0/).

Lithium-ion batteries are currently one of the most common rechargeable batteries widely used in electric vehicles, portable electronic devices, and energy storage systems. They benefit from a long lifespan, high energy density, and being lightweight [3]. However, the normal operation of lithium-ion batteries is significantly impacted by temperature. Excessive charging and discharging, internal and external short circuits, mechanical damage, and prolonged operation in high-temperature environments can all lead to battery overheating [4], accelerate the degradation of active battery materials, and affect battery life [5]. At the same time, low temperatures and high C-rate charging may also cause internal short circuits within the battery, leading to uncontrolled heating [6]. Since most of the electrolytes in present lithium-ion batteries are flammable liquids [7], excessive heat can potentially cause fire or explosion [8]. To effectively prevent the occurrence of irreversible thermal runaway [9] and ensure the safe and reliable operation of lithium-ion batteries [10], a battery thermal management system (BTMS) [11] suitable for lithium-ion batteries should be installed.

The impact of the battery pack's packaging shape [12] and cooling technique [13] on its thermal performance, as well as variations in battery voltage, current, state of charge (SOC), and other parameters, must all be taken into consideration in BTMS research. In addition to preheating the battery in a low-temperature environment [14], BTMS must prevent thermal runaway of the battery during high-rate charging [15]. Currently, researchers can effectively achieve thermal diagnosis by establishing a reliable physical model of lithium-ion batteries. These models are usually mathematical models solved by partial differential equation solving [16], to clarify the internal mechanism and provide detailed voltage [17], current, and temperature data when the battery works [18]. Based on this, many studies forecast lithium-ion battery thermal problems. A better multi-scale entropy algorithm (MSE), for instance, was developed in [19] to compute the battery health in real-time and can identify hazardous battery conditions seven days before thermal runaway. In [20], voltage increment deviation and cumulative deviation analysis are employed, together with density-based spatial clustering with noise (DBSCAN) for thermal diagnosis. This technique can identify a single battery's deterioration a few days before thermal runaway. Reference [21] considers the effects of discharge depth (DoD) and temperature on the internal heating of lithium-ion batteries and constructs a two-dimensional electrothermal model for temperature prediction of lithium-ion batteries. Reference [22] models the passive balanced battery module, and the predicted temperature data obtained can serve as a reference for BTMS design.

At present, the thermal runaway prediction method and internal short circuit (ISC) detection can theoretically effectively avoid the thermal runaway of lithium-ion batteries under normal conditions. However, in the face of unexpected events such as puncture, compression, or a sudden increase in environmental temperature, it is difficult to quickly achieve temperature warnings by establishing a model and processing complex data online. Therefore, sensor selection is an effective method to detect thermal runaways in case of an emergency. In the process of thermal runaway, many parameters can be used as early warning indicators. For example, reference [23] built an early warning system for thermal runaway energy storage stations based on sound signals. Temperature early warning is realized by observing the sound signal of battery thermal runaway discharge. This method first uses a denoising system to remove interference signals and then uses an extreme gradient boosting (XGBoost) pattern recognition classifier for acoustic signal recognition and processing. Similarly, literature [24] also carried out the diagnosis of lithium-ion battery thermal runaway based on the gas signal. The results show that these methods can accurately complete the thermal diagnosis, but the detection of thermal runaway gas signals is more suitable for large battery systems such as energy storage power stations, but not for small models. Although the internal temperature detection of lithium-ion batteries is more reliable than surface temperature detection, surface temperature detection utilizing a thermographic camera, temperature sensor, and other tools is still an efficient, convenient, and low-cost battery temperature diagnosis method [25]. This method is more intuitive and also supports online diagnosis. The distribution image of the surface temperature of lithium-ion battery is obtained through the infrared thermographic camera and other equipment, and the image is preprocessed. According to the thermal characteristics and surface temperature distribution of the battery, LBIP determine whether the lithium-ion battery has a thermal fault. The use of surface temperature imaging to determine the thermal state of lithium-ion can serve as a supplement to existing diagnostic methods.

Machine learning algorithms can automatically process large amounts of data and adaptively adjust them by analyzing the relationships between the data, which is applied in the field of batteries. For example [26], proposed a data-driven thermal fault diagnosis for electric vehicles, which detects thermal runaway units by applying discrete frechet and local anomaly factors to real-time voltage and current detection units. Reference [27] proposes a data-driven method based on single-cell voltage comparison, which achieves thermal diagnosis by analyzing dynamic data curves. This method has good robustness. Reference [28] established a lithium-ion battery thermal diagnosis network using a transformer, which is based on thermal imaging of lithium batteries. With considerable advancements in accuracy and speed, image recognition can process a lot of image data online. It is common practice to employ the instance segmentation model represented by Mask R–CNN. By extending Mask R–CNN to thermal pictures for segmentation tasks, reference [29] presents an effective technique for searching image objects that can identify heating parts that cannot be discriminated in RGB images.

As a result, our research uses instance segmentation models to apply a deep learning model to the thermal image processing of lithium batteries, recognizing and classifying thermally defective batteries. The following are the important contributions made to our research.

1. Online lithium-ion battery intelligent perception (LBIP): the model for thermal fault detection and localization was constructed, based on the Mask R–CNN instance segmentation model, and fine-tuned using a pre-trained model. Set the loss function, and optimize the network structure and network parameters in combination with the battery dataset;
2. Thermal finite element analysis: using Ansys Fluent software conducts finite element analysis on lithium-ion batteries, simulates charging and discharging as well as internal short circuit faults, and obtains surface thermal imaging images of lithium-ion batteries. Data preprocessing is performed on the images.

3. Based on the accurate detection of Mask R–CNN and the important information contained in lithium-ion thermal imaging images, a complete lithium-ion battery thermal fault diagnosis model has been established to identify and localize faulty lithium-ion batteries.
4. We evaluated the effectiveness of the LBIP using datasets from single-cell battery and 1P3S battery packs, as well as testing and validating any errors that emerged during the battery pack's real-time online operation.

The remaining content of this article is as follows: Section 2 describes the network structure of LBIP; Section 3 describes the setting of the loss function of the model; Section 4 provides experimental details and results; Section 5 summarizes the work of this article.

Nomenclature

Abbreviations

BTMS	Battery Thermal Management System
LBIP	Lithium-ion Battery Intelligent Perception
Mask R–CNN	Mask Region-based Convolutional Neural Network
FPN	Feature Pyramid Network
RPN	Region Proposal Network
ROI	Region of Interest
ROI Align	Region of Interest Align
ResNet50	Deep Residual Network with 50 layers
FCN	Fully Convolutional Network
BN	Batch Normalization
ReLU	Rectified Linear Unit
FC	Fully Connected Network
NTGK	Newman, Tiedemann, Gu, Kim battery model
SGD	Stochastic Gradient Descent
Bbox	Bounding Box
mAP	Mean Average Precision
mAR	Mean Average Recall
TP	True Positive
FP	False Positive
FN	False Negative

Variables 2

C2∼C5	The output of ResNet50 in the backbone
P2∼P6	Feature maps
x_{k+1}, y_{k+1}	The central point of the anchor projected back to the location coordinates of the original battery image.
w_{k+1}	The width of the anchor in the feature map
h_{k+1}	The height of the anchor in the feature map
dx, dy	Rectification of anchor center point coordinates
dw	Rectification of anchor width
dh	Rectification of anchor height
cls_logits	The output of the box classification task
box_prediction	The output of the box regression task
mask_fcn_logits	The output of the classification task in mask head

Variables 1

σ_+	The effective electric conductivity for the positive electrode
σ_-	The effective electric conductivity for the negative electrode
φ_+	Phase potential for the positive electrode
φ_-	Phase potential for the negative electrode
j_{short}	The current transfer rate of battery
q_{short}	The heat generation rate due to the battery's internal short-circuit
j_{ECh}	The volumetric current transfer rate of the battery
q_{ECh}	The electrochemical reaction heat
q_{absue}	The heat generation due to the thermal runaway reaction
r_c	The short-circuit resistance at the short-circuit point
Vol	The activate zone's volume of a single battery
V	The battery cell voltage
$Q_{nominal}$	The battery's total electric capacity
Q_{ref}	The reference electric capacity
T	The operating temperature of the battery

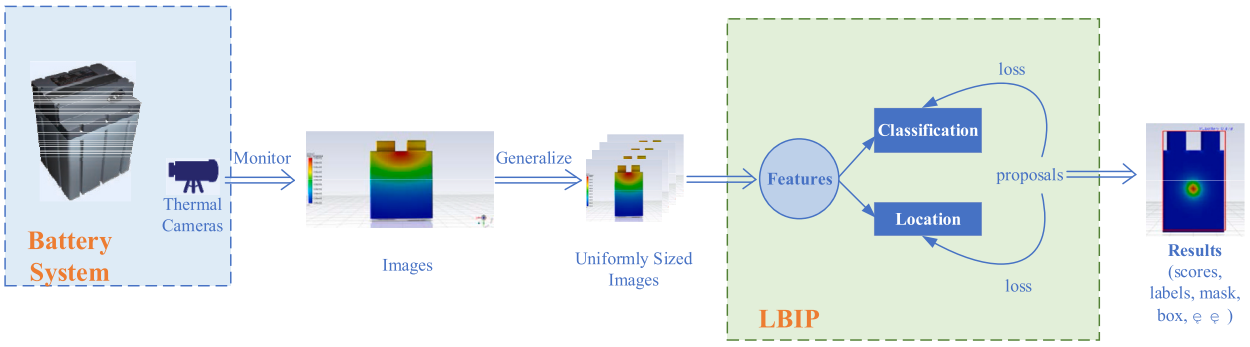

Fig. 1. The process of LBIP.

2. LBIP workflow

The lithium-ion battery system monitors the surface temperature changes of the battery in real-time through a thermal imager and saves thermal imaging images at the same time intervals. The saved surface thermal imaging images are processed in batches and cropped into uniformly sized images as input for LBIP. LBIP first extracts key point information from the image, converts it into digital signals, and inputs them into the network. Then, it propagates the extracted information forward for complete classification, recognition, and localization. LBIP calculates the error between the generated proposals and the true value and performs backpropagation to continuously reduce the error before outputting the recognition result. The process of LBIP is shown in Fig. 1.

We used commercial software Ansys Fluent to construct the dataset and perform finite element analysis on lithium-ion batteries. To identify the internal failure site in the damaged battery, we created a small area and applied a very low resistance to it. Afterward, patch the area onto the cell body of the battery to simulate the internal short circuit of the battery.

We selected labelme to label the thermal imaging image we obtained. Each image has a mark indicating the various battery operating conditions. At the same time, export the.json file generated by labelme to obtain a mask image, and use the original image and mask image together as input for LBIP.

3. LBIP network structure

In LBIP, the Mask R–CNN is a two-stage object detection network that was developed by He et al. [30], based on the Faster R–CNN in 2017 [31]. It excels in the recognition and segmentation of objects within images. The network is composed of five main components, which include the backbone and FPN (Feature Pyramid Network), RPN (Region Proposal Network), ROI Align (Region of Interest Align), FCN (Fully Convolutional Network), and mask branch. Fig. 2 showcases the layout of the network.

A. Multiscale Thermal Perception

After normalized processing, the images are obtained and inputted into the network. A backbone network is a convolutional neural model used for feature extraction, which is responsible for extracting image feature parameters and generating feature maps. In this paper, the pre-trained ResNet50 is selected as the backbone structure, which can significantly reduce the training time of the model and enhance the model's performance.

FPN mainly solves the problem of multi-scale detection in target detection. Although deep backbone network generates high-level feature maps providing rich semantic information, they have limited resolution and preserve minimal object location information, which makes it difficult to do frame regression afterward. To enhance the efficacy of object detection and semantic segmentation, the FPN network may extract numerous scale features from a picture and integrate them. Fig. 3 illustrates the backbone network and FPN structures.

In our research, ResNet50 and FPN are combined to extract multiscale thermal information. ResNet50 features a four-layer structure, and the output feature diagram of each layer is denoted as C2, C3, C4, and C5, respectively. The FPN network makes the output channel size of the feature graph of each layer consistent (channel = 256) after 1×1 convolution. After up-sampling and down-sampling, the feature maps of different layers are fused and the final feature maps are output, which are respectively denoted as P2, P3, P4, P5, and P6.

B. Global Search

RPN network uses feature maps to generate proposals, that is, to predict several proposals in the input image, and output the proposals of the target region and the corresponding score.

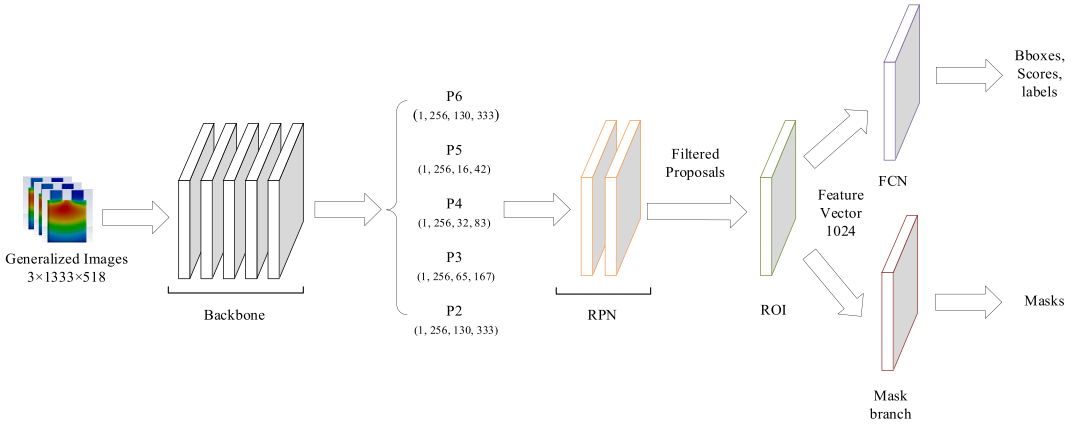

Fig. 2. The network structure of LBIP.

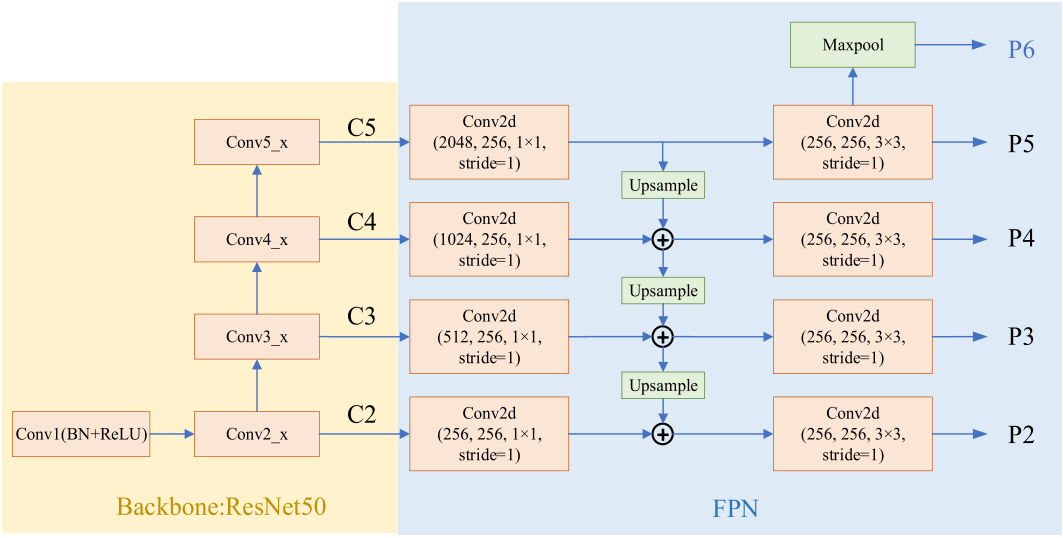

Fig. 3. The composition of backbone network and the construction of FPN.

For the part of the proposals, the RPN network generates numerous anchors in advance and obtains the correction value based on the network regression parameter after abandoning the anchors that exceed the boundary. After that, each anchor's center and width are adjusted to make sure that it is appropriately close to the ground truth. In our research, anchor operation is carried out based on the five-layer feature map of P2~P6 in multi-scale thermal perception (P1 does not participate in anchor generation). A 4n-dimensional vector can be obtained by regressing the feature vectors in each layer, which can be used to describe the generated n anchors. The correction formula of the anchor is as follows [30]:

$$x_{k+1} = (1 + dx) \cdot x_k \tag{1}$$

$$y_{k+1} = (1 + dy) \cdot y_k \tag{2}$$

$$w_{k+1} = \exp(dw) \cdot w_k \tag{3}$$

$$h_{k+1} = \exp(dh) \cdot h_k \tag{4}$$

where w and h are the width and height of the anchor, and x and y are the central point of the anchor projected back to the location coordinates of the original image. The correction for rectification is dx, dy, dw, and dh.

For the regression part, the RPN network outputs the front and back view confidence for n proposals. A large number of boxes are generated after anchor correction, and then the non-maximum value is used to suppress filtering according to the scores of boxes to obtain relatively accurate proposals.

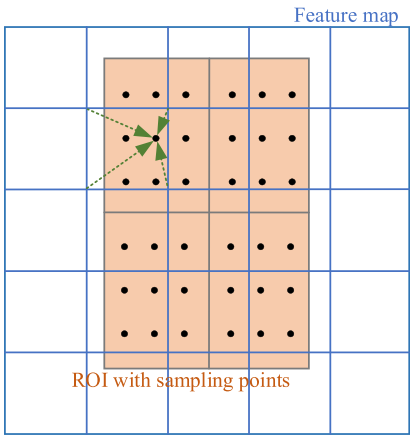

Fig. 4. ROI Align calculation.

C. Fine-grained Localization

The ROI part is responsible for feature extraction of ROI (Region of Interest) generated by the RPN network. The proposals generated by the RPN network will be calculated through ROI Align and mapped to the corresponding feature maps. The ROI Align algorithm uses bilinear interpolation to calculate the mapped ROI coordinates (x, y, w, h) and then processes these ROIs into a unified size through pooling, facilitating subsequent border classification, regression, and prediction of Mask. ROI Align with bilinear interpolation is more precise than the first ROI Pooling process. Fig. 4 shows the calculation of ROI Align. It calculates the sampling point position in ROI through adjacent pixels on the feature map. The sampling points are ultimately used for pooling calculations.

The feature map of uniform size processed by ROI Align then passes through full connection layers and a softmax layer for box classification and regression. The ROI structure is depicted in Fig. 5. The cls_logits include the classification of the ROI, while box_prediction includes the location and confidence level of the ROI.

In parallel with box regression, the mask branch continues to process the created ROI. The mask branch determines whether a given pixel in the ROI region is part of the instance, and finally outputs the binary mask of the target instance. This study's Mask R–CNN uses an FPN structure, pooling the ROI output before performing a convolution operation to produce the location. Fig. 6 depicts the mask branch's structure.

D Network Improvement

We also refer to the work in reference [32] and build the LBIP-V1 and LBIP-V2 networks in Pytorch. LBIP-V2 first performs batch normalization on convolutions in FPN. After processing the same batch of feature maps, a distribution with a mean of 0 and a variance of 1 is obtained.

LBIP-V2 has made the following improvements compared to LBIP-V1.

Firstly, the BN layer is placed behind the convolutional layer, making the network more prone to convergence. The BN layer is also added after the convolutional layer in the mask branch. The improved backbone structure is shown in Fig. 7.

Secondly, LBIP-V2 has added a convolutional layer to the RPN network.

Thirdly, to improve feature extraction for the ROI region, four layers of convolution with BN layers are utilized directly in place of the two linear layers in LBIP-V1. Fig. 8 shows the structure of ROI heads in LBIP-V2.

4. LBIP testing and verification

A Data Acquisition and Processing

We used commercial software Ansys to carry out finite element simulations of lithium-ion batteries. We set up three models for testing: a single-cell battery, a 1P3S battery pack, and a flattened 1P3S battery pack model. The parameters of the lithium battery model refer to Kim et al.'s paper [33]. Table 1 lists the specific parameters of the lithium-ion model.

In the Table 1, C-Rate represents the discharge rate, which is the hourly rate of battery discharge. A positive value represents the

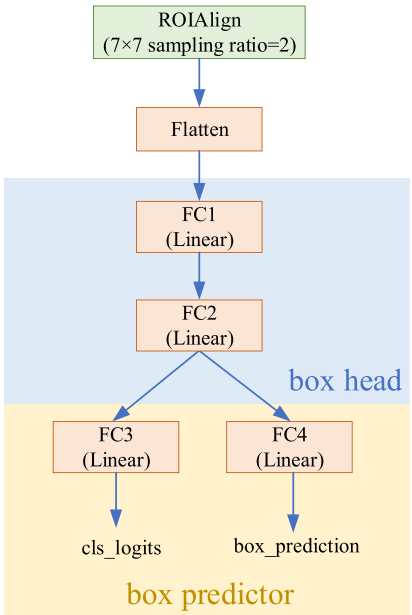

Fig. 5. The structure of ROI.

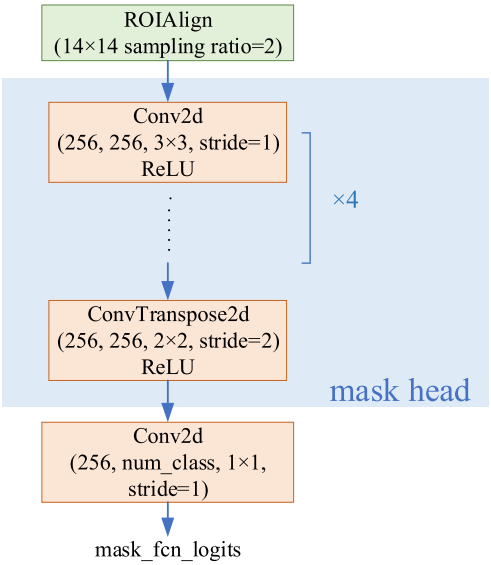

Fig. 6. The structure of Mask branch.

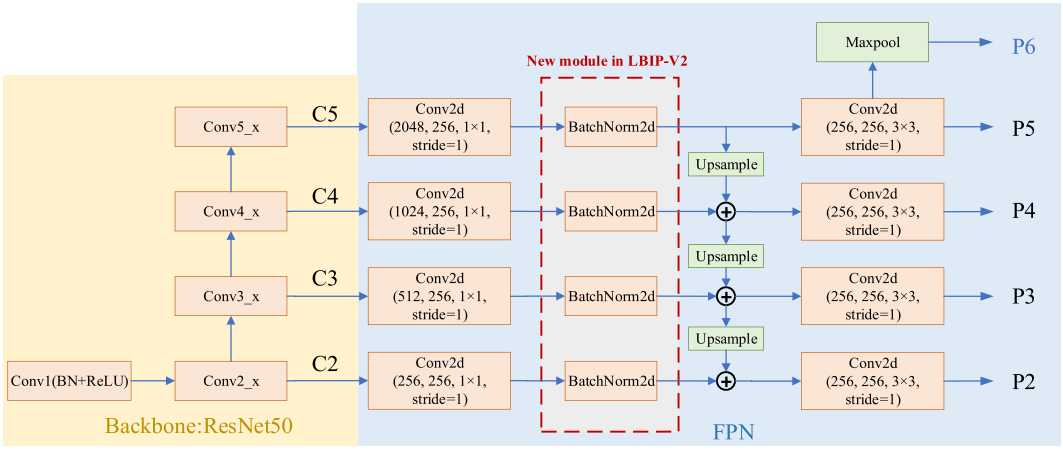

Fig. 7. The composition of backbone network and the construction of FPN (LBIP-V2).

discharge rate, while a negative value represents the charging rate. C-rate is numerically equivalent to the charging and discharging current ratio of the rated battery capacity. The system can currently be specified during simulation. The discharge current is represented by a positive system current, and the charging current is represented by a negative system current. The system voltage can be specified to represent the potential of the anode when the cathode potential is 0V. Similarly, when specifying the system power, it means that the battery model will charge and discharge at a specified digital constant power.

The NTGK model [34] provided by Fluent was used to solve the operating conditions of the battery under multiple operating conditions. In Ansys Fluent, we used the MSMD [35] solution method to determine the temperature distribution within the length range of lithium-ion batteries. The heat generation formula of the model is given by the following series of formulas:

$$\frac{\partial \rho C_p T}{\partial t} - \nabla \cdot (k \nabla T) = \sigma_+ |\nabla \varphi_+|^2 + \sigma_- |\nabla \varphi_-|^2 + q_{ECh} + q_{short} + q_{absue} \tag{5}$$

$$\nabla \cdot (\sigma_+ \nabla \varphi_+) = j_{short} - j_{ECh} \tag{6}$$

$$\nabla \cdot (\sigma_- \nabla \varphi_-) = j_{ECh} - j_{short} \tag{7}$$

where σ_+ and σ_- are the effective electric conductivities for the positive and negative electrodes, φ_+ and φ_- are phase potentials for the positive and negative electrodes. j_{ECh} and q_{ECh} are the volumetric current transfer rate and the electrochemical reaction heat, respectively. j_{short} and q_{short} are the current transfer rate and heat generation rate due to the battery's internal short-circuit,

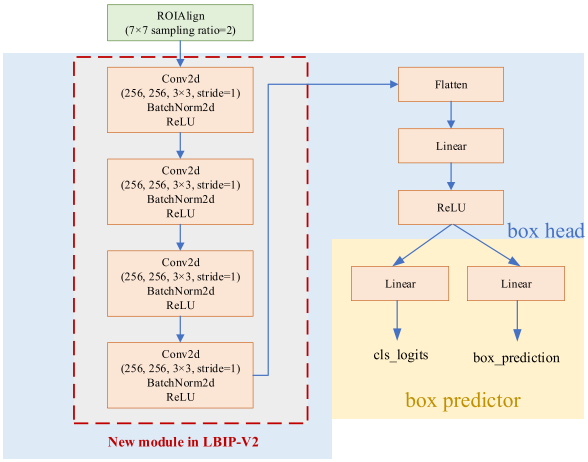

Fig. 8. The structure of ROI (LBIP-V2).

Table 1
The parameters of NTGK lithium battery.

Project	Parameter
Cathode Material	$LiFePO_4$
Anode Material	graphite
Capacity	14.6Ah
C-rate	1 (−1 during charging)
System Current (A)	1
System Voltage (V)	4
System Power (W)	60 (200 during 1P3S battery pack model)
External Resistance (ohm)	1
Min. Stop Voltage (V)	3
Max. Stop Voltage (V)	4.3

respectively. q_{absue} is the heat generation due to the thermal runaway reactions under the thermal abuse condition. Under usual battery operation, q_{absue} is set to 0. j_{short} and q_{short} are all set to 0 without internal short circuits.

When the battery experiences an internal short circuit fault, the calculation of j_{short} and q_{short} is as follows:

$$j_{short} = a(\varphi_+ - \varphi_-) / r_c \tag{8}$$

$$q_{short} = a(\varphi_+ - \varphi_-)^2 / r_c \tag{9}$$

where r_c is the short-circuit resistance at the short-circuit point, a is a constant. Therefore, a/r_c can represent the degree of short circuit at the short-circuit point.

For the selected NTGK model, the default parameters come from Ref. [34]. The calculation formulas for j_{ECh} and q_{ECh} are:

$$j_{ECh} = \frac{Q_{nominal}}{Q_{ref} Vol} Y[U - V] \tag{10}$$

$$q_{ECh} = j_{ECh}\left[U - V - T\frac{dU}{dT}\right] \tag{11}$$

where *Vol* represents the activated zone's volume of a single battery. *V* is the battery cell voltage. In MSMD solution, *V* can be calculated as $\varphi_+ - \varphi_-$. $Q_{nominal}$ is the battery total electric capacity. Q_{ref} is the capacity of the battery that is used in experiments to obtain the model parameters *Y* and *U*.

Y and *U* are functions of battery depth of discharge (DoD):

$$DoD = \frac{Vol}{3600 Q_{nominal}} \int_0^t j dt \tag{12}$$

$$U = \left(\sum_{n=0}^{5} a_n (DoD)^n \right) - C_2 \left(T - T_{ref} \right) \tag{13}$$

$$Y = \left(\sum_{n=0}^{5} b_n (DoD)^n \right) \exp\left(- C_1 \left(\frac{1}{T} - \frac{1}{T_{ref}} \right) \right) \tag{14}$$

where C_1 and C_2 are the battery-specific NTGK model constants. T is the operating temperature of the lithium-ion battery. During the simulation process, both the discharge depth DoD and the reference battery capacity need to be manually adjusted and the values are also from Ref. [34].

For dataset generation, the simulation step was set to 30100 steps, and the temperature changes of the lithium battery were monitored to obtain the image.

Secondly, we simulated the temperature changes of a single-cell battery model with a capacity of 14.6 Ah under three different operating conditions: 1C charging, 1C discharging, and internal short circuit. The single-cell battery model dataset consisted of 48 images and was divided into 3 groups based on charging, discharging, and internal short circuit conditions, with 16 images in each group. Among them, 13 images were for training and 3 images were for validation. We randomly selected 26 partial temperature images from the first 50 % seconds of the discharge state and the last 50 % seconds of the charging state, and randomly selected them from the internal short-circuit fault image set to ensure the randomness of the dataset selection. Fluent software is used to simulate the failure of cells 1, 2, and 3 for the 1P3S battery pack model, correspondingly. Similar to the single-cell battery model, a total of 48 thermal images—16 for each of the three failure scenarios—were randomly chosen while creating the dataset for the 1P3S battery model. Finally, for the flattened 1P3S battery pack model, the dataset contained 112 pictures in total, which also included cases of cell 1 failure, cell 2 failure, cell 3 failure, and multiple cell simultaneous failures. We set up the testing dataset using the same method and randomly selected images from both the non-training and validation datasets. The settings for the three datasets are shown in Table 2.

B LBIP Network Structure in Battery Dataset

The overall network structure of LBIP processing is shown in Fig. 9.

Taking the 1P3S dataset as an example, the thermal image size of the original battery is 417 × 1074 (Width × Height), an RGB image. After resizing, batch process the images into 3 × 1333 × 518 (C × H × W). At the same time, the bounding box is also scaled accordingly. The scaled images are packed into a batch and input into the network, which contains the image itself and target information. The above operation corresponds to the transform section in Fig. 9, which preprocesses the size of the image.

The preprocessed images are scaled to 1/4, 1/8, 1/16, and 1/32 of the original size through a backbone network. After downsampling, feature maps from different layers are fused to output P2~P6 feature maps. The feature map is processed by the RPN head and anchor generator to obtain anchors. The anchor sizes set in LBIP are respectively 32 × 32, 64 × 64, 128 × 128, 256 × 256, and 512 × 512, and the aspect ratios of anchors are 0.5, 1.0, and 2.0, respectively. For each pixel in the feature map, 15 anchors of different sizes are generated. Table 3 shows the size of the feature map and the number of anchors.

In RPN, cls_ logits and boxes_ pred are used for classification and regression, ultimately obtaining the anchor's predicted target score and (*dx, dy, dw, dh*) regression parameters. The final output of the RPN network is a proposal set, which is filtered to leave about 2000 proposals before entering the second stage of object detection.

Proposals will generate a feature vector with a size of 1024 after processing in the ROI section, and outputting the final box predictions and mask branches.

C. Results of a Single-Cell Battery Dataset

We built the Mask R–CNN model using Pytorch and specified the learning rate, momentum weight, and weight decay of SGD. Here, we tested two different LBIP models: LBIP-V1 and LBIP-V2, and the network structure of these two is described in Section III.

Meanwhile, we also selected pre-training model fine-tuning and used the random gradient descent SGD method to update weight parameters during the training process. To stop model oscillations during the initial training process, it also used the warm-up learning rate approach to boost the learning rate from a low learning rate to a fixed learning rate for training. The learning rate and results of the loss variations in different areas of the network during training are depicted in Fig. 10 (a)-(e).

The training loss of LBIP-V2 is shown in Fig. 10. After 10 epochs, the total loss of the network decreased to around 0.05, the mask loss decreased to 0.04, the RPN loss decreased to within 0.02, and the bbox loss decreased to 0.01.

We chose the evaluation indicators for the COCO dataset [36], where Precision, Recall, and F1Score are calculated as follows:

Table 2
The composition of three datasets.

Dataset	Total	Training	Validation	Testing
Single-cell battery model	48	39	9	9
1P3S battery pack model	48	39	9	9
Flattened 1P3S battery pack model	112	91	21	21

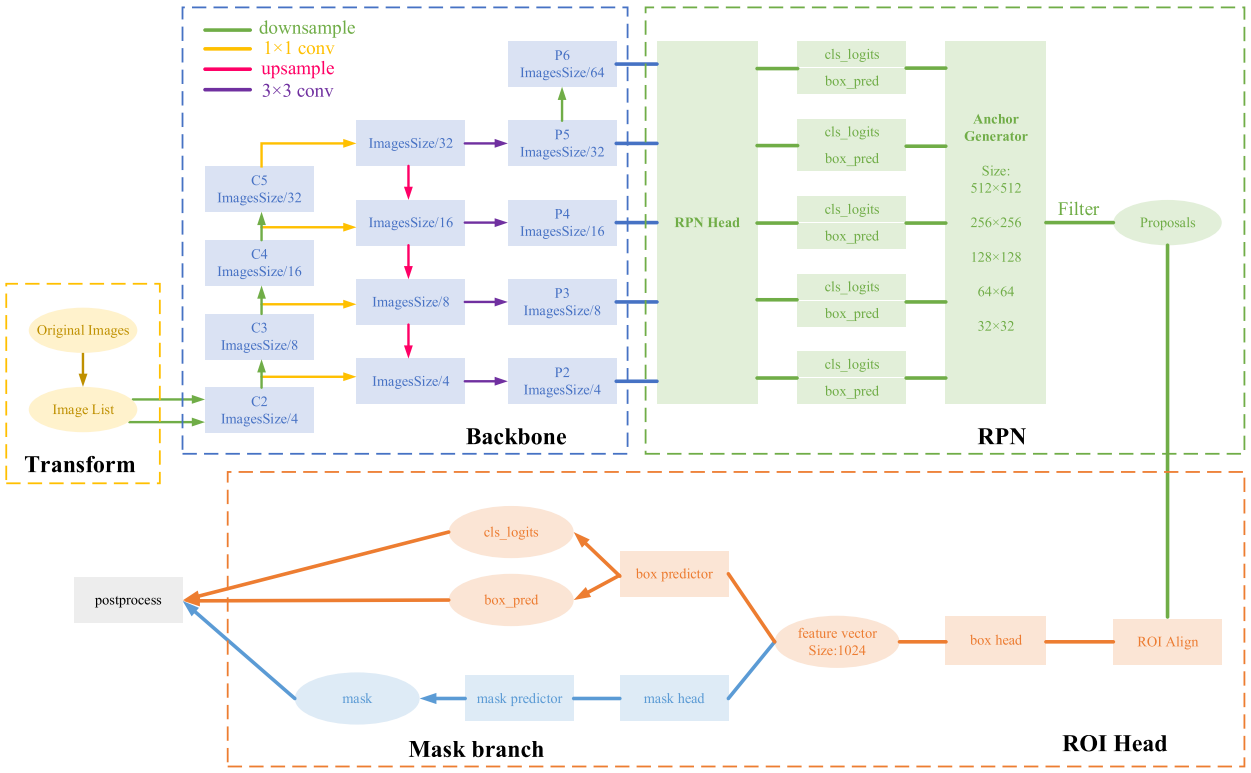

Fig. 9. LBIP network.

Table 3
Size of feature map and number of anchors.

Feature Map	Size	Number of Anchors
P2	(1, 256, 130, 333)	$130 \times 333 \times 15 = 649350$
P3	(1, 256, 65, 167)	$65 \times 167 \times 15 = 162825$
P4	(1, 256, 32, 83)	$32 \times 83 \times 15 = 39840$
P5	(1, 256, 16, 42)	$16 \times 42 \times 15 = 10080$
P6	(1, 256, 8, 21)	$8 \times 21 \times 15 = 2520$

$$\text{Precision} = \frac{TP}{FP + TP}$$

$$\text{Recall} = \frac{TP}{TP + FN}$$

$$\text{F1Score} = 2 \times \frac{\text{Precision} \times \text{Recall}}{\text{Precision} + \text{Recall}}$$

During the training process of a single battery dataset, the mAP (Mean Average Precision) and mAR (Mean Average Recall) in validation are shown in Fig. 11 (a) and (b).

The results of a single-cell battery dataset are as follows in Table 4.

In the validation dataset, it can be seen from Table 4 that the mAP of the network for bounding boxes is nearly 0.94 in LBIP-V1, while the mAP in segmentation is nearly 0.95. F1Score also remains a high score of about 0.94 both in the bounding box and segmentation. The performance of the LBIP-V2 is slightly inferior. The bounding box mAP values remain around 0.78, which is approximately 0.2 lower than the results of the LBIP-V1. Similarly, the mAR value remains around 0.8, which is 0.15–0.16 lower than the LBIP-V1. The F1score values do not exceed 0.80, indicating that for a single-cell battery dataset, the LBIP-V1 performs better than LBIP-V2. Similarly, in the segmentation task, the mAP, mAR, and F1Score of LBIP-V2 are all about 0.04–0.05 lower than those of LBIP-V1.

Meanwhile, there is a slight decrease in the performance of LBIP-V1 and LBIP-V2 in the testing dataset. However, the mAP, mAR, and F1Score of LBIP-V1 all exceed 0.91 in both bounding box and segmentation. The accuracy of a small network is higher in a

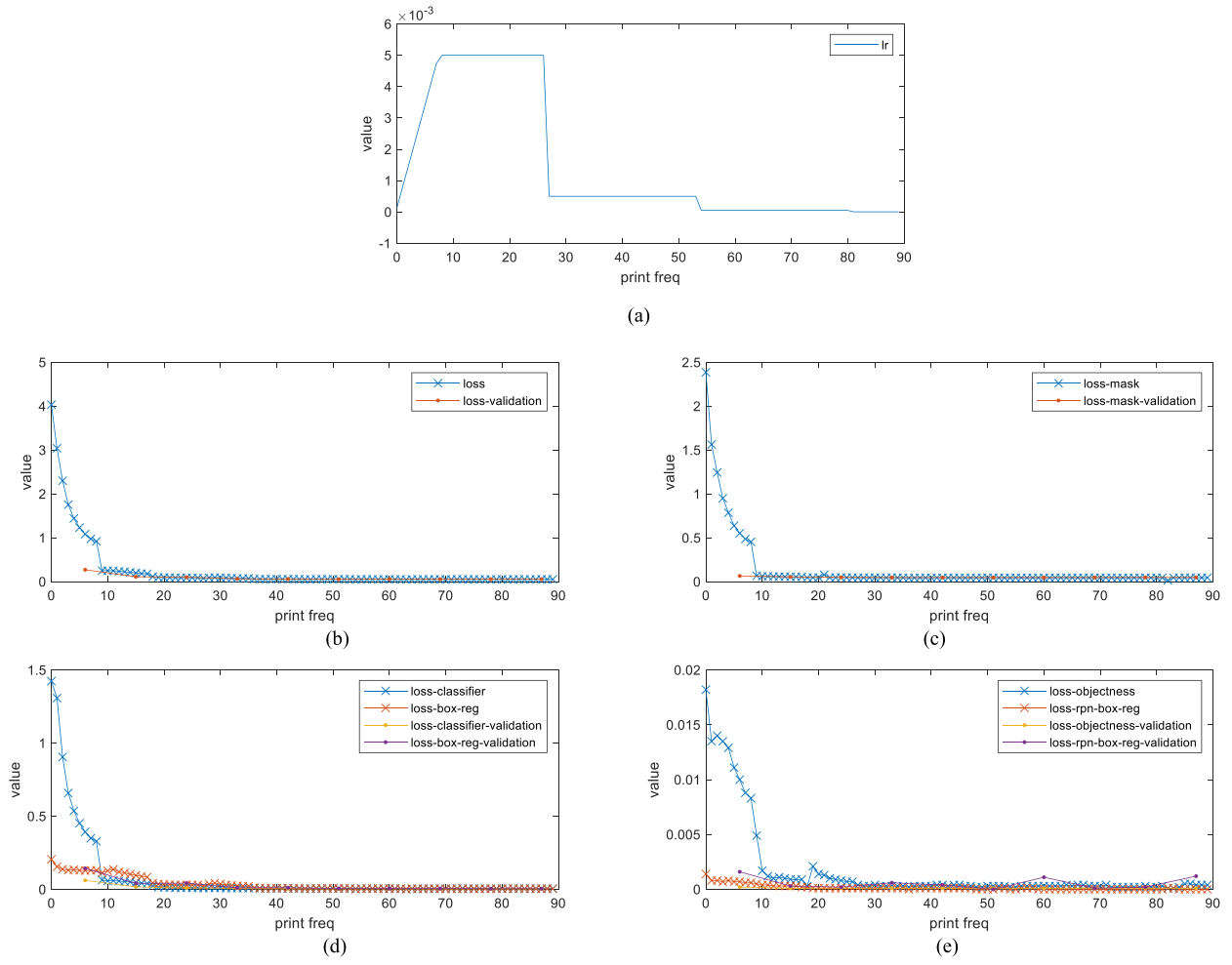

Fig. 10. The training loss of LBIP-V2. (a) is the lr in training; (b) is the total loss of the model; (c) is the loss of mask branch; (d) is the Bbox loss which consists of loss-classifier and loss-box-reg; (e) is the RPN loss which consists of loss-objectness and loss-rpn-box-reg.

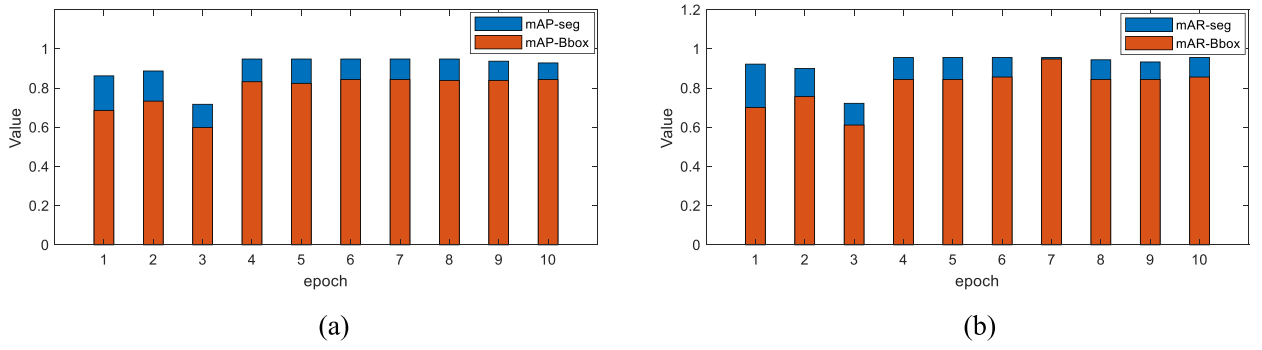

Fig. 11. Single-cell battery dataset model evaluation. (a) is the mAP in the segmentation and bounding box tasks. (b) is the mAR value in the segmentation and bounding box tasks.

relatively simple detection task. In both validation and testing, the performance of the segmentation task seems better than the bounding box task and mAR is higher than mAP for LBIP.

Fig. 12 (a)-(c) shows the prediction box, prediction mask area, and the overlap between the predicted mask area and ground truth of the network. The label of the short-circuit battery in the dataset is P_Battery, the charging status is marked as C_Battery, discharge status is marked as D_Battery. It can be seen that the proposed LBIP-V1 has good performance in distinguishing three working

Table 4
Performance of single cell battery dataset.

Dataset	Network		Score	mAP	mAR	F1Score
Validation	LBIP-V1	bounding box	>0.940	0.937	0.944	0.940
		segmentation		0.948	0.956	0.952
	LBIP-V2	bounding box	>0.863	0.774	0.789	0.781
		segmentation		0.904	0.911	0.907
Testing	LBIP-V1	bounding box	>0.940	0.911	0.911	0.911
		segmentation		0.918	0.922	0.920
	LBIP-V2	bounding box	>0.797	0.852	0.856	0.854
		segmentation		0.878	0.878	0.878

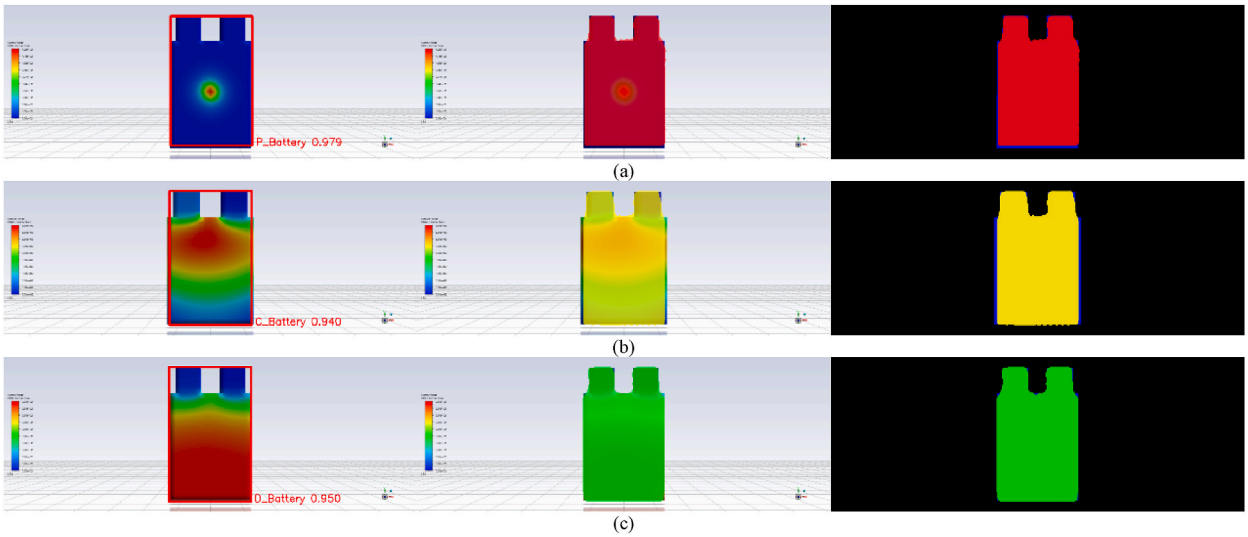

Fig. 12. The classification results of LBIP-V1 in single battery images. The results include the label, prediction area, and score which represents the confidence of a certain class of targets in the bounding box. (a) is a short-circuit battery perceptual result. (b) is a charging battery perceptual result. (c) is a discharging battery perceptual result.

conditions and localizing the faulty battery.

D. Results of the 1P3S Battery Pack Dataset

Similarly, we conducted experiments on the 1P3S battery pack. Labels cell_1, cell_2, and cell_3 represent faults in cell 1, cell 2, and cell 3 of the 1P3S battery pack, respectively. The diagnostic results of the 1P3S battery pack are shown in Fig. 13 (a)-(c).

Table 5 shows the performance of the 1P3S battery pack dataset. In the validation dataset, the bounding box task's mAP, mAR, and F1Score all hit 1 for the 1P3S dataset, whereas the segmentation's mAP, mAR, and F1Score all came in at 0.867 using LBIP-V1. Similarly, the LBIP-V1 still performs better than LBIP-V2 both in validation and testing. It can be indicated that LBIP still performs well for diagnosing thermal faults in battery packs or several batteries.

E. Results of the Flattened 1P3S Battery Pack Dataset

We flattened the 1P3S model in Ansys Workbench and saved the thermal images from a frontal position to better illustrate the temperature variations of a single lithium-ion battery pack cell during internal short circuit faults. The network will recognize and choose batteries in the dataset that have intrinsic short-circuit issues.

Fig. 14 (a)-(c) shows the results of flattened 1P3S battery pack images using the larger network (LBIP-V2). The results demonstrate that LBIP-V2 has a very high short circuit detection score of over 0.985 for the flattened battery model. Table 6 shows the performance of the flattened 1P3S battery pack dataset.

It can be seen that the large network performs slightly better in flattened models than the small one, probably due to the large number of flattened model datasets. The recognition confidence levels of LBIP-V1 and LBIP-V2 on both the testing and validation datasets exceeded 0.98, demonstrating the accuracy of the model.

By vertically comparing the results of the single-cell battery, 1P3S battery pack, and flattened 1P3S battery pack model datasets, the scores of the detection boxes for both network structures gradually increase as the datasets become richer. Each network can accurately

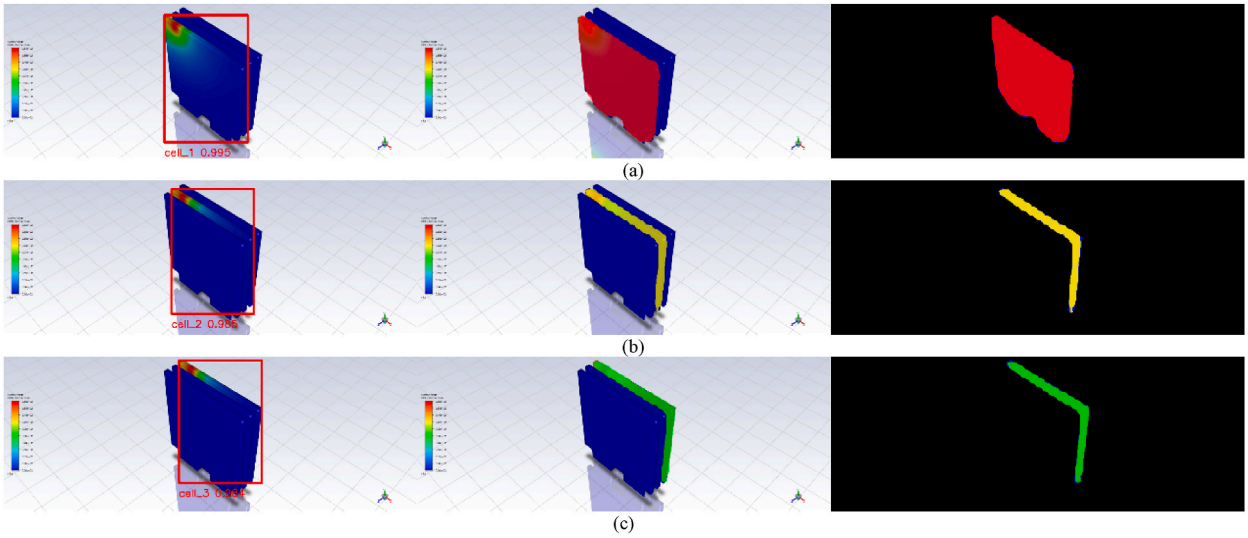

Fig. 13. The classification results of LBIP-V1 in 1P3S battery images. The results include the label, prediction area, and score which represents the confidence of a certain class of targets in the bounding box. (a) is perceptual short-circuit cell 1 in a 1P3S battery pack. (b) is perceptual short-circuit cell 2 in a 1P3S battery pack. (c) is perceptual short-circuit cell 3 in 1P3S battery pack.

Table 5
Performance of 1P3S battery pack dataset.

Dataset	Network		Score	mAP	mAR	F1Score
Validation	LBIP-V1	bounding box	>0.983	1	1	1
		segmentation		0.867	0.867	0.867
	LBIP-V2	bounding box	>0.977	0.789	0.789	0.789
		segmentation		0.833	0.833	0.833
Testing	LBIP-V1	bounding box	>0.980	1	1	1
		segmentation		0.844	0.844	0.844
	LBIP-V2	bounding box	>0.956	0.830	0.833	0.831
		segmentation		0.855	0.856	0.855

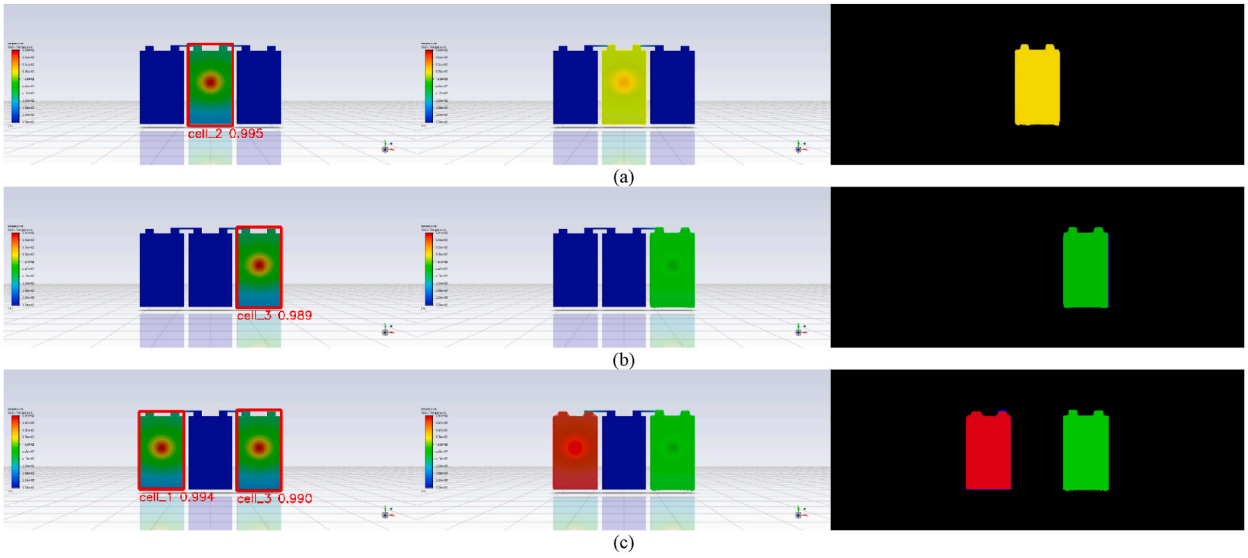

Fig. 14. The classification results of LBIP-V2 in flattened 1P3S battery pack images. The results include the label, prediction area, and score which represents the confidence of a certain class of targets in the bounding box. (a) is perceptual short-circuit cell 2 in a flattened 1P3S battery pack. (b) is perceptual short-circuit cell 3 in a flattened 1P3S battery pack. (c) is perceptual short-circuit in cell 1 and cell 3 in a flattened 1P3S battery pack.

Table 6
Performance of flatten 1P3S battery pack dataset.

Dataset	Network		Score	mAP	mAR	F1Score
Validation	LBIP-V1	bounding box	>0.978	0.983	0.989	0.986
		segmentation		0.990	0.994	0.992
	LBIP-V2	bounding box	>0.981	0.984	0.989	0.986
		segmentation		0.979	0.986	0.982
Testing	LBIP-V1	bounding box	>0.987	0.972	0.980	0.976
		segmentation		0.991	0.993	0.992
	LBIP-V2	bounding box	>0.989	0.973	0.981	0.977
		segmentation		0.993	0.994	0.993

identify battery cells with abnormal temperature rise caused by internal short circuit issues. Large networks will perform better when dealing with big datasets.

F. Results of Battery Pack's Real-time Online Operation

We tested LBIP on images of the battery running online. The 1P3S battery pack flattening model was still selected, and Ansys Fluent was selected to simulate the discharge of the battery pack at the rate of 1C. The simulation duration is a total of 15 min. The battery pack is in normal operation for 0–5 min, battery cell 1 experiences an internal short circuit fault due to external force for 5–10 min, and battery cell 3 experiences an internal short circuit fault due to external force for 10–15 min. Fig. 15 shows this process.

The simulation obtains a battery thermal imaging image approximately every 0.95 s, resulting in a total of 944 thermal images. Considering the large dataset, we chose LBIP-V2 for thermal fault identification, and the identified results are shown in Fig. 16 (a)-(d).

From the results, it can be seen that LBIP-V2 has a confidence of over 0.98 for online battery fault diagnosis, and LBIP can respond promptly in the event of a thermal fault in the battery, demonstrating excellent online performance. The diagnostic time of LBIP on V100GPU is 20.95fps, and online diagnosis has good real-time performance.

5. Results and discussion

Our research developed a computer vision-based lithium-ion battery intelligent perception (LBIP) model and improved network parameters based on the lithium-ion battery dataset. LBIP includes LBIP-V1 and LBIP-V2, which are used for small datasets and big datasets, respectively. We chose Resnet50 as the backbone network, built the Mask R–CNN network using Pytorch, and implemented FPN. We constructed the mask branch and calculated the losses for RPN, bbox, and mask branches. Ansys Fluent is used to generate experimental datasets and simulate the thermal imaging of lithium-ion batteries under three different conditions: **a single-cell battery**, **a 1P3S battery pack**, and **a flattened 1P3S battery pack model**. Our method has shown that the model has a diagnostic recall and accuracy of 0.95 for thermal faults in lithium-ion batteries under various operating conditions. In addition, the highest F1Score value of LBIP-V2 exceeds 0.98. At the same time, we conducted tests on real-time lithium-ion battery packs. During sequential operation, LBIP was able to quickly and accurately identify the location of the faulty battery when the battery cell experienced a thermal failure due to an unexpected event, with a score exceeding 0.910. The experimental results demonstrate the feasibility of LBIP.

Funding statement

This research was supported by the project of National Natural Science Foundation of China (U23B6006, 52277116).

Data availability statement

Data will be made available on request.

CRediT authorship contribution statement

Luyu Tian: Writing – original draft, Visualization, Validation, Methodology, Investigation, Data curation, Conceptualization. **Chaoyu Dong:** Writing – review & editing, Visualization, Validation, Supervision, Methodology, Formal analysis, Data curation,

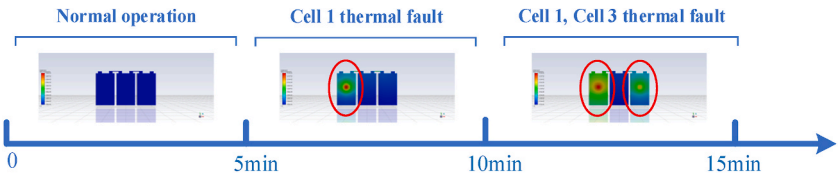

Fig. 15. The real-time online simulation of the battery pack.

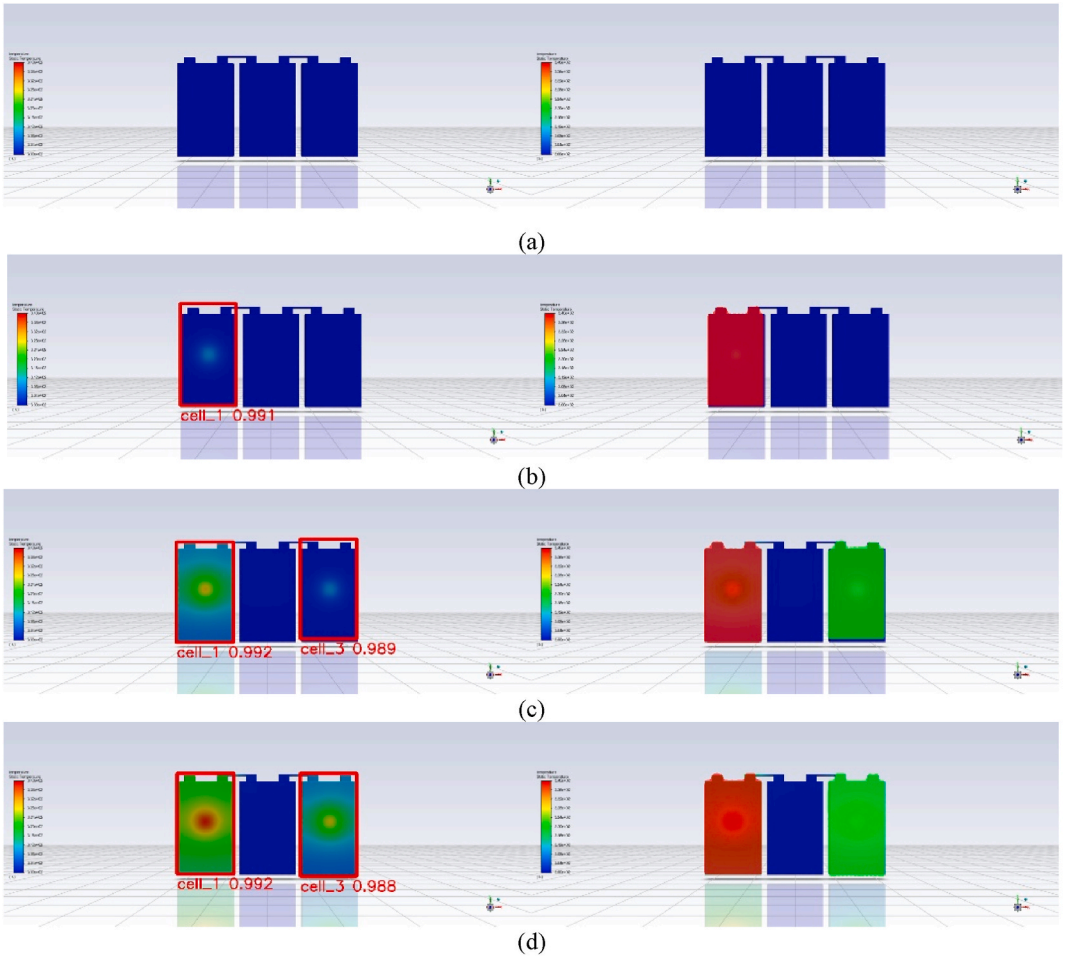

Fig. 16. The classification results of LBIP-V2 in battery pack's real-time online operation. The results include the label, prediction area, and score which represents the confidence of a certain class of targets in the bounding box. (a) is the perceptual result of LBIP on the surface thermal imaging of lithium-ion batteries under normal operating conditions within 0–5 min. (b) is the perceptual result of LBIP on the surface thermal imaging of cell 1 thermal fault within 5–10 min. (c) is the perceptual result of LBIP on the thermal imaging of cell 1 and cell 3 thermal fault within 10–14 min. (d) is the perceptual result of LBIP on the thermal imaging of cell 1 and cell 3 thermal fault in the last 1 min (14–15min).

Conceptualization. **Yunfei Mu:** Supervision, Resources, Project administration, Investigation. **Xiaodan Yu:** Supervision, Resources, Project administration, Investigation. **Hongjie Jia:** Supervision, Resources, Project administration, Investigation.

Declaration of competing interest

The authors declare that they have no known competing financial interests or personal relationships that could have appeared to influence the work reported in this paper.

Appendix A

A. 1. LBIP Loss Formulation

The loss of LBIP in this paper consists of three parts [30]:

$$Loss = L_{rpn} + L_{bbox} + L_{mask} \tag{A.1}$$

where total loss is the sum of RPN network loss L_{rpn}, bounding box loss L_{bbox} and mask branch loss L_{mask}.

A.1.1 RPN Loss

The loss of the RPN network consists of RPN classification loss and RPN regression loss. BCE Loss (Binary cross entropy Loss) is selected for classification loss.

$$L_{rpn-cls} = -\left[p_i^* \log(p_i) + \left(1 - p_i^*\right)\log(1 - p_i)\right] \tag{A.2}$$

RPN regression loss is calculated as follows:

$$L_{rpn-reg} = \sum_i smooth_{L_1}\left(t_i - t_i^*\right) \tag{A.3}$$

Therefore, the total loss of the RPN network is:

$$L_{rpn} = \frac{1}{N_{cls}}\sum_i L_{rpn-cls}\left(p_i, p_i^*\right) + \lambda\frac{1}{N_{reg}}\sum_i p_i^* L_{rpn-reg}\left(t_i, t_i^*\right) \tag{A.4}$$

For classification loss, N_{cls} is the sample number. p_i is the predicted probability of anchor i being an object; p_i^* is 1 for positive samples and 0 for negative samples. For regression loss, N_{reg} is the number of anchor position information, t_i is the boundary regression parameter of the i-th anchor, and t_i^* is the gt-box corresponding to the i-th anchor. λ is equal to 10.

A.1.2 Bounding-box Loss

Bbox loss is also composed of classification loss and regression, namely:

$$L_{bbox} = L_{bbox-cls}(p, u) + \lambda[u \geq 1]L_{bbox-loc}(t^u, v) \tag{A.5}$$

where p is softmax probability distribution predicted by the classifier; u is the label corresponding to the real category of the target; t^u is the regression parameter of the corresponding category u of bounding box regression prediction. v is the bounding box regression parameter corresponding to the true target. When the ROI region is a positive sample, $u = 1$ and $[u \geq 1] = 1$, otherwise, $[u \geq 1] = 0$.

The classification loss in (A.6) is softmax cross entropy loss:

$$L_{bbox-cls} = -\log p_u \tag{A.6}$$

where p_u is the probability that the classifier predicts the true class u.

Regression loss is calculated as:

$$L_{bbox-loc} = \sum_{i\in\{x,y,w,h\}} smooth_{L_1}\left(t_i^u, v_i\right) \tag{A.7}$$

A.1.3 Mask Branch Loss

The mask branch has an output of $K \times m \times m$ dimension for each ROI region, and K masks of $m \times m$ size are encoded during loss calculation. There are K categories for each ROI. Corresponding to an ROI belonging to the K-th class in the ground truth, L_{mask} is defined only on the K-th mask. L_{mask} is calculated using the BCE Loss (Binary Cross Entropy loss) method. BCE Loss is widely used in multi-label classification tasks. The formula for the loss function is as follows:

$$L_{mask} = \frac{1}{m^2}\sum_i^K [k \geq 1]\sum_1^{m^2}\left[-y * \log(sigmoid(x)) - (1 - y) * \log(1 - sigmoid(x))\right] \tag{A.8}$$

In the formula, y represents the label value of the mask of the current location. The positive sample is $y = 1$, and the negative sample is $y = 0$. x is the output value of the current position, and sigmoid function transformation is performed. If the kth channel corresponds to the real category of the target, $k = 1$, $[k \geq 1] = 1$, otherwise, $[k \geq 1] = 0$.

References

[1] C Dong, J Wang, X Li, C Jin, W Jiang, Z Zhang, et al., Synthetic resilience exploration and economic defense strategy for microgrid-level AC/DC hybrid energy system, IEEE Trans. Power Electron. 38 (2023) 2565–2576.

[2] C Dong, R Chu, T Morstyn, MD McCulloch, H Jia, Online rolling evolutionary decoder-dispatch framework for the secondary frequency regulation of time-varying electrical-grid-electric-vehicle system, IEEE Trans. Smart Grid 12 (2021) 871–884.

[3] M.K. Tran, C. Cunanan, S. Panchal, R. Fraser, M. Fowler, Investigation of individual cells replacement concept in lithium-ion battery packs with analysis on economic feasibility and pack design requirements, Processes 9 (2021).

[4] M.-K. Tran, M. Fowler, A review of lithium-ion battery fault diagnostic algorithms: current progress and future challenges, Algorithms 13 (2020).

[5] M.-K. Tran, S. Panchal, T.D. Khang, K. Panchal, R. Fraser, M. Fowler, Concept review of a cloud-based smart battery management system for lithium-ion batteries: feasibility, logistics, and functionality, Batteries-Basel. 8 (2022).

[6] X. Feng, M. Ouyang, X. Liu, L. Lu, Y. Xia, X. He, Thermal runaway mechanism of lithium ion battery for electric vehicles: a review, Energy Storage Mater. 10 (2018) 246–267.

[7] Y. Xie, H. Li, W. Li, Y. Zhang, M. Fowler, M.K. Tran, et al., Improving thermal performance of battery at high current rate by using embedded heat pipe system, J. Energy Storage 46 (2022).
[8] M. Keyser, A. Pesaran, Q.B. Li, S. Santhanagopalan, K. Smith, E. Wood, et al., Enabling fast charging - battery thermal considerations, J. Power Sources 367 (2017) 228–236.
[9] X.H. Zhang, Z. Li, L.A. Luo, Y.L. Fan, Z.Y. Du, A review on thermal management of lithium-ion batteries for electric vehicles, Energy (2022) 238.
[10] N. Ghaeminezhad, Z.S. Wang, Q. Ouyang, A review on lithium-ion battery thermal management system techniques: a control-oriented analysis, Appl. Therm. Eng. (2023) 219.
[11] Q. Wang, B. Jiang, B. Li, Y.Y. Yan, A critical review of thermal management models and solutions of lithium-ion batteries for the development of pure electric vehicles, Renewable Sustainable Energy Rev. 64 (2016) 106–128.
[12] L.K. Singh, R. Kumar, A.K. Gupta, A. Sharma, S. Panchal, Computational study on hybrid air-PCM cooling inside lithium-ion battery packs with varying number of cells, J. Energy Storage 67 (2023) 107649.
[13] Z. Feng, J. Zhao, C. Guo, S. Panchal, Y. Xu, J. Yuan, et al., Optimization of the cooling performance of symmetric battery thermal management systems at high discharge rates, Energy & Fuels, 2023.
[14] V. Talele, U. Moralı, M.S. Patil, S. Panchal, K. Mathew, Optimal battery preheating in critical subzero ambient condition using different preheating arrangement and advance pyro linear thermal insulation, Therm. Sci. Eng. Prog. 42 (2023) 101908.
[15] Y. Fan, Z. Wang, X. Xiong, S. Panchal, R. Fraser, M. Fowler, Multi-objective optimization design and experimental investigation for a prismatic lithium-ion battery integrated with a multi-stage Tesla valve-based cold plate, Processes 11 (2023) 1618.
[16] W.X. Mei, C. Liang, J.H. Sun, Q.S. Wang, Three-dimensional layered electrochemical-thermal model for a lithium-ion pouch cell, Int. J. Energy Res. 44 (2020) 8919–8935.
[17] J.C. He, M.S. Hosen, R. Youssef, T. Kalogiannis, J. Van Mierlo, M. Berecibar, A lumped electro-thermal model for a battery module with a novel hybrid cooling system, Appl. Therm. Eng. (2023) 221.
[18] Y. Xie, W. Li, Y. Yang, F. Feng, A novel resistance-based thermal model for lithium-ion batteries, Int. J. Energy Res. 42 (2018) 4481–4498.
[19] J. Hong, Z. Wang, F. Ma, J. Yang, X. Xu, C. Qu, et al., Thermal runaway prognosis of battery systems using the modified multiscale entropy in real-world electric vehicles, Ieee Transactions on Transportation Electrification 7 (2021) 2269–2278.
[20] D. Li, Z. Zhang, P. Liu, Z. Wang, DBSCAN-based thermal runaway diagnosis of battery systems for electric vehicles, Energies 12 (2019).
[21] S. Vashisht, D. Rakshit, S. Panchal, M. Fowler, R. Fraser, Thermal behaviour of li-ion battery: an improved electrothermal model considering the effects of depth of discharge and temperature, J. Energy Storage 70 (2023) 107797.
[22] R. Baveja, J. Bhattacharya, S. Panchal, R. Fraser, M. Fowler, Predicting temperature distribution of passively balanced battery module under realistic driving conditions through coupled equivalent circuit method and lumped heat dissipation method, J. Energy Storage 70 (2023) 107967.
[23] T. Su, N. Lyu, Z. Zhao, H. Wang, Y. Jin, Safety warning of lithium-ion battery energy storage station via venting acoustic signal detection for grid application, J. Energy Storage 38 (2021).
[24] J. Klink, A. Hebenbrock, J. Grabow, N. Orazov, U. Nylen, R. Benger, et al., Comparison of model-based and sensor-based detection of thermal runaway in li-ion battery modules for automotive application, Batteries-Basel. 8 (2022).
[25] T. Manh-Kien, M. Fowler, Sensor fault detection and isolation for degrading lithium-ion batteries in electric vehicles using Parameter Estimation with Recursive Least Squares, Batteries-Basel. 6 (2020).
[26] Z.Y. Sun, Z.P. Wang, P. Liu, Z.A. Qin, Y. Chen, Y. Han, et al., An online data-driven fault diagnosis and thermal runaway early warning for electric vehicle batteries, IEEE Trans. Power Electron. 37 (2022) 12636–12646.
[27] M. Schmid, H.-G. Kneidinger, C. Endisch, Data-driven fault diagnosis in battery systems through cross-cell monitoring, IEEE Sensor. J. 21 (2021) 1829–1837.
[28] M.R. Li, C.Y. Dong, B.Y. Xiong, Y.F. Mu, X.D. Yu, Q. Xiao, et al., STTEWS: a sequential-transformer thermal early warning system for lithium-ion battery safety, Appl. Energy (2022) 328.
[29] H.C. Song, M.S. Knag, T.E. Kimg, Object Detection based on Mask R-CNN from infrared camera, Journal of Digital Contents Society 19 (6) (2018) 1213–1218.
[30] K. He, G. Gkioxari, P. Dollar, R. Girshick, Ieee. Mask R-CNN. 16th IEEE International Conference on Computer Vision (ICCV), 2017, pp. 2980–2988. Venice, ITALY.
[31] S. Ren, K. He, R. Girshick, J. Sun, R.-C.N.N. Faster, Towards real-time object detection with region proposal networks, IEEE Trans. Pattern Anal. Mach. Intell. 39 (2017) 1137–1149.
[32] Y. Li, S. Xie, X. Chen, P. Dollar, K. He, R. Girshick, Benchmarking detection transfer learning with vision transformers, 2021 arXiv preprint arXiv:211111429.
[33] U.S. Kim, J. Yi, C.B. Shin, T. Han, S. Park, Modeling the dependence of the discharge behavior of a lithium-ion battery on the environmental temperature, J. Electrochem. Soc. 158 (2011) A611.
[34] K.H. Kwon, C.B. Shin, T.H. Kang, C.-S. Kim, A two-dimensional modeling of a lithium-polymer battery, J. Power Sources 163 (2006) 151–157.
[35] G.-H. Kim, K. Smith, K.-J. Lee, S. Santhanagopalan, A. Pesaran, Multi-domain modeling of lithium-ion batteries encompassing multi-physics in varied length scales, J. Electrochem. Soc. 158 (2011) A955.
[36] COCO Common Objects in Context. https://cocodataset.org/#detection-eval.